

Channel-specific angular distributions of HCl and CH₃ products from the reaction of atomic chlorine with stretch-excited methane

Zee Hwan Kim, Hans A. Bechtel, and Richard N. Zare^{a)}

Department of Chemistry, Stanford University, Stanford, California 94305-5080

(Received 12 April 2002; accepted 21 May 2002)

A beam containing methane and molecular chlorine is expanded into a vacuum where the methane is excited with two quanta of C–H stretching (one quantum each in two of the four C–H bonds). The reaction is initiated by fast Cl atoms generated by photolysis of Cl₂ at 355 nm, and the resulting CH₃ and HCl products are detected in a state-specific manner using resonance-enhanced multiphoton ionization. Speed-dependent spatial anisotropies (β_{prod}) of HCl and CH₃ products allow identification of three major product channels. They are in order of importance: (a) HCl ($v=0$) + CH₃ [ν_1 (symmetric stretch) or ν_3 (asymmetric stretch) = 1]; (b) HCl ($v=1$) + CH₃ [ν_2 (umbrella bend) = 1]; and (c) HCl ($v=1$) + CH₃ ($\nu_1=1$). The CH₃ ($v=0$) product cannot be detected, and the HCl ($v=2$) product is minor. Channels (a) and (c) proceed in a vibrationally adiabatic manner, whereas channel (b) appears to involve the nonadiabatic interaction involving the low frequency bending mode in methane that correlates to the bending mode in the methyl radical product. The angular distributions differ markedly for the three product channels. This behavior is explained by the propensity for reactive collisions involving H-atom transfer along the line of centers and the difference in the cones of acceptance. The rotational angular momentum vector of the HCl ($v=1, J=1$) product is aligned perpendicular to the line of centers, which is consistent with an impulsive energy release along the line of centers. Our results clearly demonstrate that the direct and local mode picture of the chemical reaction remains largely valid, which connects vibrational excitation to the scattering dynamics. © 2002 American Institute of Physics. [DOI: 10.1063/1.1493192]

I. INTRODUCTION

Because polyatomic molecules have more than one mode of vibration, it is important to compare one vibrational mode of the reagent to another in influencing reactivity and in controlling product state distributions in bimolecular reactions. The concepts of mode and bond selectivity have been experimentally examined in only a few simple reaction systems thus far,^{1,2} and much work remains to be done to explore this topic.

We have investigated the reaction of atomic chlorine with vibrationally excited methane. This reaction provides an excellent opportunity to explore the above-mentioned aspects of a vibrationally activated reaction. The Cl + CH₄ reaction produces CH₃, a polyatomic product, so that we can investigate the vibrational energy disposal among the vibrational modes of “old bonds” (CH₃) as well as the “new bond” (HCl). As in the case of the reaction of H atoms with vibrationally excited H₂O,^{3,4} recent work on the reaction of Cl atoms with stretch-excited CH₄ shows that the reactivity enhancement upon vibrational excitation is localized in a C–H bond.⁵ Furthermore, Kim *et al.* have reported strong mode specificity and bond selectivity in the reaction of atomic chlorine with methane (CH₄, CH₂D₂, and CHD₃) excited to its first C–H stretch overtone. Only the activated C–H bond within the partially deuterated methane takes part

in the reaction, and the pattern of the vibrational excitation of the methyl radical indicates that the reaction proceeds without major energy redistribution of the initial vibrational motion of the methane reagent.

In this paper, we report the results of a more detailed investigation of the reaction,



in which the methane is prepared in its asymmetric stretch vibration, one quantum each in two of its four C–H oscillators. The focus of this study is twofold. First, we investigate the correlated vibrational energy partitioning between HCl and CH₃ products in order to probe how and where the initial vibrational energy is channeled. Second, the state-resolved differential cross sections and the product rotational polarization are studied to understand the scattering dynamics of this reaction. Our results lead us to propose a simple model to explain the correlation of the angular distribution, the energy release, and the rotational alignment of the HCl product.

II. BACKGROUND

A. IR spectroscopy of methane near 6000 cm⁻¹

The first overtone transition of the triply degenerate ν_3 (asymmetric stretching) mode of methane is composed of A_1 , F_2 , and E symmetry species. Among them, only the excited states with F_2 symmetry [$2\nu_3(F_2)$] are allowed by one-photon IR excitation. The stretching modes of CH₄ have

^{a)}Author to whom correspondence should be addressed. Electronic mail: zare@stanford.edu

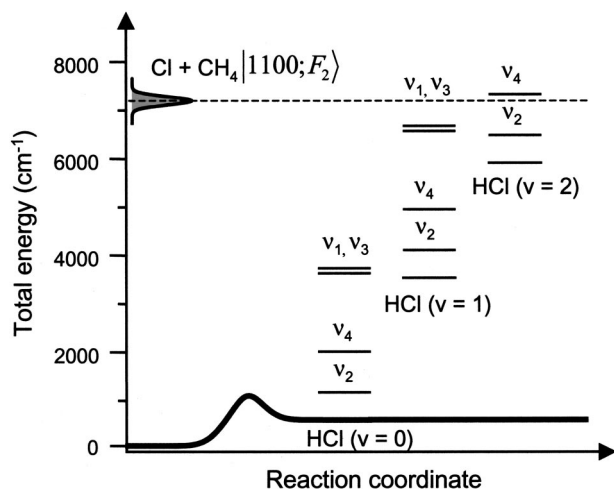


FIG. 1. Schematic energetics of the reaction $\text{Cl} + \text{CH}_4(1100;F_2) \rightarrow \text{HCl} + \text{CH}_3$. The collisional energy spread is represented by a Gaussian distribution estimated using the formulas of van der Zande *et al.* (Ref. 35). Also shown on the right-hand side of the reaction coordinate are the fundamental frequencies of the CH₃ normal modes superimposed on top of the vibrational levels of HCl.

some bending character owing to the Fermi resonance between one stretching quantum and two bending quanta. In fact, a rigorous description of this eigenstate requires a polyad approach that takes into account the interactions between vibrational states.^{6,7} Extensive spectroscopic and theoretical studies on this subject can be found in Refs. 6–11. In particular, theoretical modeling of the IR spectra by Halonen and Child,⁹ and Halonen¹⁰ showed that the $2\nu_3(F_2)$ eigenstate is dominated by C–H stretching local mode character that corresponds to the assignment $|1100;F_2\rangle$ (one stretching quantum in each of two C–H oscillators) with approximately a 10% contribution from bending. Without a knowledge of methane reactivity associated with excitation of the bending mode, the bending mode contribution to the $2\nu_3(F_2)$ eigenstate could cause difficulty in interpreting the reactivity. Recent results by Kim *et al.*,⁵ however, clearly show the dominant role of stretching character in the reaction of stretch-excited methane with atomic chlorine.

B. Energetics

This reaction is slightly endothermic ($\Delta H^0 = 660 \text{ cm}^{-1}$), and the estimated reaction barrier is $\sim 1000 \text{ cm}^{-1}$ (Ref. 12) (see Fig. 1). The 355 nm photolysis of Cl₂ provides $1200 \pm 100 \text{ cm}^{-1}$ of center-of-mass (CM) collision energy (E_{coll}), and the vibrational excitation of CH₄ supplies an extra 6000 cm^{-1} of energy. Hence the total available energy is 7200 cm^{-1} , which is well above the reaction threshold. Also shown in Fig. 1 are the energy levels of HCl and CH₃ products in various vibrational states [for CH₃, the normal modes shown are ν_1 (symmetric stretch, 3004 cm^{-1}), ν_2 (umbrella bending, 610 cm^{-1}), ν_3 (asymmetric stretch, 3160 cm^{-1}), and ν_4 (deformation, 1400 cm^{-1})]. The fundamental vibrational frequencies of HCl and the C–H stretching modes of CH₃ are close in energy (HCl, 2991 cm^{-1} ; CH₃, $\nu_1 = 3004 \text{ cm}^{-1}$, $\nu_3 = 3160 \text{ cm}^{-1}$). Also, the ν_2 bend of CH₃ and the reaction endothermicity are similar. Consequently,

the product channels HCl ($v=1$) + CH₃ (ν_1 or $\nu_3=1$) and HCl ($v=2$) + CH₃ ($v=0$ or $\nu_2=1$) have similar energetics. Likewise, the HCl ($v=1$) + CH₃ ($v=0$ or $\nu_2=1$) and the HCl ($v=0$) + CH₃ (ν_1 or $\nu_3=1$) channels are nearly isoenergetic. Figure 1 illustrates that this reaction presents an interesting opportunity to compare the relative propensity toward the nearly isoenergetic product channels.

C. Methodology

The procedures for obtaining the differential cross sections (DCS), the spatial anisotropies, and the angle-resolved alignment were described in previous publications.^{13–15} We present only a brief outline of the methods. The core-extracted time-of-flight (TOF) profiles taken with parallel (I_{\parallel}) and perpendicular (I_{\perp}) photolysis polarization with respect to the TOF axis can be converted to isotropic $I_{\text{iso}} = I_{\parallel} + 2I_{\perp}$ and anisotropic $I_{\text{aniso}} = 2(I_{\parallel} - I_{\perp})$ components. The isotropic component contains information on the laboratory speed distribution ($d\sigma/dv_{\text{prod}}$). This speed distribution can be uniquely transformed into the DCS ($d\sigma/d\cos\theta$) with the knowledge of the internal energy of the unobserved product. The internal energy of the unobserved product (hereafter, called co-product) can be determined by measuring the spatial anisotropy of the observed product $\beta_{\text{prod}}(v)$ which is related to the kinematics of the photoinitiated reaction by

$$\beta_{\text{prod}}(v) = \beta_{\text{phot}} P_2(\cos\theta_u). \quad (2)$$

In Eq. (2) P_2 is the second-order Legendre polynomial, θ_u is the angle between the center of mass (CM) velocity and the product laboratory velocity, as determined uniquely by the internal energies of the reagents, products, and the reaction enthalpy, and β_{phot} is the spatial anisotropy associated with the photodissociation step for the Cl-atom precursor.¹⁶ The $\beta_{\text{prod}}(v)$ for the HCl product in a particular ro-vibrational state contains information on the internal excitation of the CH₃ that is produced *in coincidence* with that particular HCl product. Likewise, $\beta_{\text{prod}}(v)$ of the state-selected CH₃ product has information on the internal energy of the HCl co-product. Therefore, these complementary measurements reveal detailed features of the correlated energy disposal between HCl and CH₃ products as well as providing information needed for converting the speed distribution to a DCS.

For the analysis and interpretation of the rotational polarization of HCl ($v=1, J=1$), we use the stationary-target frame (STF)¹³ in which the z axis (quantization axis) is parallel to the laboratory velocity of the product, and the y axis is defined to be normal to the scattering plane. The spatial averaging associated with the STF→LAB frame transformation partially washes out the off-diagonal moments [$A_1^{(2)}$ (STF) and $A_2^{(2)}$ (STF)] of the reaction product, and the degree of this averaging depends on the kinematics and the CM scattering angle. On the other hand, the $A_0^{(2)}$ (STF) moment is not averaged out by the frame transformation. In our experiment, only 10% of the off-diagonal moments survive the spatial averaging. In spite of repeated attempts, it was not possible to obtain TOF profiles with sufficient signal-to-noise ratio to extract all the moments. Therefore, we neglect the

off-diagonal contributions in our analysis of the rotational alignment HCl ($v=1$, $J=1$) product. This simplification is an excellent approximation for the forward and sideways scattered regions, but it becomes less rigorous in the backward scattered direction.

III. EXPERIMENT

A 1:4:5 mixture of molecular chlorine (Matheson, research grade, 99.999%), methane (Matheson, research purity, 99.999%), and helium (liquid carbonic, 99.995%) gas is supersonically expanded into the extraction region of a linear Wiley–McLaren time-of-flight (TOF) spectrometer under single-collision conditions. Photodissociation of Cl_2 with linearly polarized 355 nm light produces fast (1.6 km/s) ground-state ($^2P_{3/2}$) Cl atoms via the Cl_2 $\text{C}^1\Pi(1_u)-\text{X}^1\Sigma(0_g^+)$ transition with a spatial anisotropy, $\beta_{\text{phot}} = -1$.¹⁶ Methane is excited to the $|1100; F_2\rangle$ state (Q -branch band head) with 1.6 μm radiation. After a 60–100 ns time delay for the reaction to occur, HCl or CH_3 products are state selectively ionized by 2 + 1 resonance-enhanced multiphoton ionization (REMPI). The resulting ions subsequently drift along the TOF tube, and are detected by Chevron-type microchannel plates. The reactive signal from the vibrationally excited methane is distinguished from background (such as HCl impurity and reactive signal from the ground-state methane) by subtracting the signal with and without IR excitation on an every-other-shot basis.

The linearly polarized 355 nm photolysis beam is generated by frequency tripling the fundamental of the Nd:YAG laser output (~ 100 mJ, PL9020, Continuum). The IR radiation at 1.6 μm is obtained by parametrically amplifying (in a LiNbO_3 crystal) 3.3 μm radiation that was generated by difference-frequency mixing of 1.06 μm radiation (Nd:YAG fundamental output) and the output of a dye laser (ND6000, Continuum; LDS768, Exciton) in another LiNbO_3 crystal. The probe light for REMPI is generated by frequency doubling (in a BBO crystal) the output of a dye laser (FL2002, Lambda Physik) pumped by a Nd:YAG laser (DCR-2A, Spectra Physics). For HCl detection, we use Exciton LDS489; for CH_3 detection, we use an exciton DCM/LD698 mix. The photolysis, IR, and probe beams are focused and spatially overlapped with the supersonic expansion using f.l. = 50 cm lenses.

The rotational distributions of the HCl products are obtained by a method similar to that of Simpson *et al.*¹⁵ For the detection of HCl ($v=2$) products, we use the R -branch lines of the (1, 2) band of the HCl $F^1\Delta-X^1\Sigma^+$ transition.¹⁷ Correction factors that are needed to convert the integrated signal to the population were determined by a separate IR–REMPI double resonance experiment on HCl ($v=0$) impurities present in our expansion (see the Appendix).

A photoelastic modulator (PEM-80, Hinds International Inc.) flips the linear polarization direction of the photolysis laser between parallel and perpendicular to the TOF axis on an every-other-shot basis. The isotropic $\mathbf{I}_{\text{iso}} = \mathbf{I}_{\parallel} + 2\mathbf{I}_{\perp}$ and anisotropic $\mathbf{I}_{\text{aniso}} = 2(\mathbf{I}_{\parallel} - \mathbf{I}_{\perp})$ components of the TOF profiles are used to extract the speed-dependent spatial anisotropy of the products $\beta_{\text{prod}}(v)$ by fitting these components to basis

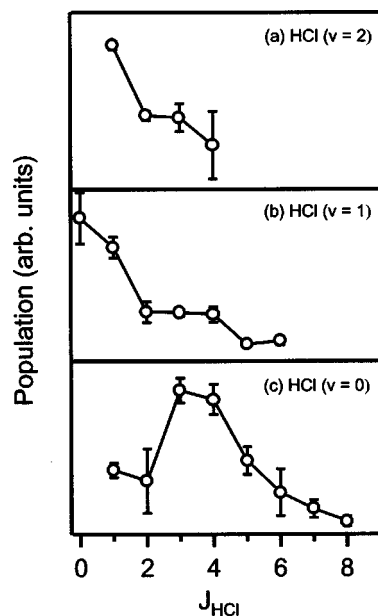


FIG. 2. Rotational distributions of HCl ($v=0$), HCl ($v=1$), and HCl ($v=2$) products. For HCl ($v=0$, $J=0$), the interference from the supersonically cooled HCl ($v=0$, $J=0$) impurity prevented us from separating the reaction signal from the background. For HCl ($v=2$, $J=0$) state, an adequate transition was not available. The error bars represent $2\sigma_{n-1}$ of replicate measurements.

functions generated by a Monte Carlo simulation. During the measurement of the alignment moment, $A_0^{(2)}$ (STF), of HCl ($v=1$, $J=1$) products, the PEM is placed in the probe laser path, and the polarization of the photolysis beam is set perpendicular to the TOF axis. The core-extracted TOF profiles with probe polarization parallel ($\mathbf{I}_{\parallel}^{\text{probe}}$) and perpendicular ($\mathbf{I}_{\perp}^{\text{probe}}$) to the TOF axis are recorded, and the isotropic $\mathbf{I}_{\text{iso}}^{\text{probe}} = \mathbf{I}_{\parallel}^{\text{probe}} + 2\mathbf{I}_{\perp}^{\text{probe}}$ and the anisotropic $\mathbf{I}_{\text{aniso}}^{\text{probe}} = 2(\mathbf{I}_{\parallel}^{\text{probe}} - \mathbf{I}_{\perp}^{\text{probe}})$ components are used to extract the angle-resolved $A_0^{(2)}$ (STF) moment after correcting for the hyperfine depolarization ($G^{(2)} = 0.25$).¹⁸

IV. RESULTS

A. HCl and CH_3 product state distributions

The product state distributions of HCl ($v=0$), HCl ($v=1$), and HCl ($v=2$) are shown in Fig. 2. We are unable to record the populations for HCl ($v=0$, $J=0$) and HCl ($v=2$, $J=0$) states because of significant interference from HCl ($v=0$, $J=0$) impurities and because of the lack of an isolated transition for detecting HCl ($v=2$, $J=0$) via the (1, 2) band of the $F-X$ transition. Rotational distributions for each vibrational manifold are very cold. The rotational energy only accounts for a small percentage of the total energy available for the reaction (see Table I). A slight decrease in average rotational excitation with vibrational excitation of HCl is also observed. The vibrational branching obtained by integrating each of the rotational distributions shows that most of the products are produced in HCl ($v=0$) (69.0%) and HCl ($v=1$) (30.9%), with an almost negligible (0.1%) contribution from HCl ($v=2$).

TABLE I. Vibrational state branching ratio and the average rotational energies.

ν	Relative vibrational state population (%)	Average rotational energy (cm ⁻¹)
0	69.0	213
1	30.9	79
2	0.1	73

Figure 3 presents the 2+1 REMPI spectrum of methyl radical products obtained using the $3p_z^2 A_2''-X^2 A_2''$ transition. Two striking features of this spectrum are the near absence of the 0_0^0 band and the appearance of a strong band at $59\,903\text{ cm}^{-1}$ corresponding to the Q -branch band head of the symmetric stretching band (1_1^1).^{19,20} A short progression in the umbrella bending mode (2_1^1 and 2_2^2 bands) is also evident. We estimate an upper bound of 3% for the population ratio of CH₃ ($\nu=0$) to CH₃ ($\nu_2=1$), using the calculated ratio of Franck–Condon factors for 2_0^0 versus 2_1^1 transitions²¹ [$q(2_0^0)/q(2_1^1)=1.125$], together with the assumption that the predissociation and ion-fragmentation rates associated with the 2_1^1 band 2_0^0 are the same.

B. Speed distributions and the spatial anisotropies of CH₃ and HCl products

Figure 4 shows the TOF profiles of CH₃ obtained from the 1_1^1 and 2_1^1 bands. The TOF profile of CH₃ ($\nu_1=1$) shows a sharp peak near time zero, with broad features on both sides. The speed distribution [Fig. 5(a)] is energetically allowed for both HCl ($\nu=0$) and HCl ($\nu=1$) channels, but the formation of HCl ($\nu=2$) co-products is energetically not possible. Figure 5(b) shows the measured spatial anisotropy of CH₃ ($\nu_1=1$) compared with the expected curves, $\beta[v; \text{HCl}(\nu=0) + \text{CH}_3(\nu_1=1)]$ and $\beta[v; \text{HCl}(\nu=1) + \text{CH}_3(\nu_1=1)]$. The spatial anisotropy follows the $\beta[v; \text{HCl}(\nu=1) + \text{CH}_3(\nu_1=1)]$ curve at lower velocities, whereas it converges to the $\beta[v; \text{HCl}(\nu=0) + \text{CH}_3(\nu_1=1)]$

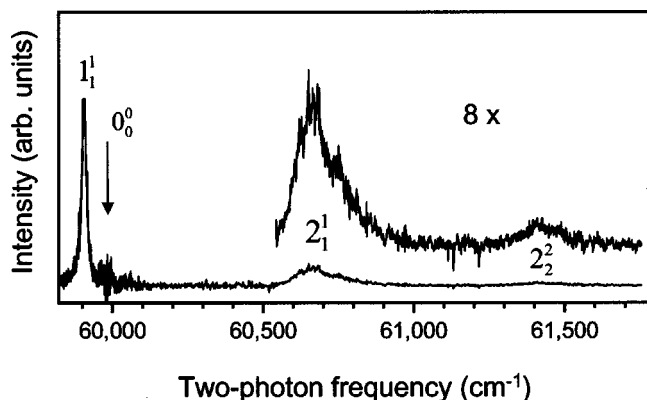


FIG. 3. 2+1 REMPI spectrum of the CH₃ product via the $3p_z-X$ transition. Also shown are the band assignments and the expected position of the 0_0^0 band. The increased noise near the 0_0^0 band position is caused by the large resonant background signal at the 0_0^0 band originating from the ground-state reaction $[\text{Cl} + \text{CH}_4(\nu=0) \rightarrow \text{HCl} + \text{CH}_3(\nu=0)]$ that generates mostly vibrationless methyl products, which does not depend on the presence of IR radiation.

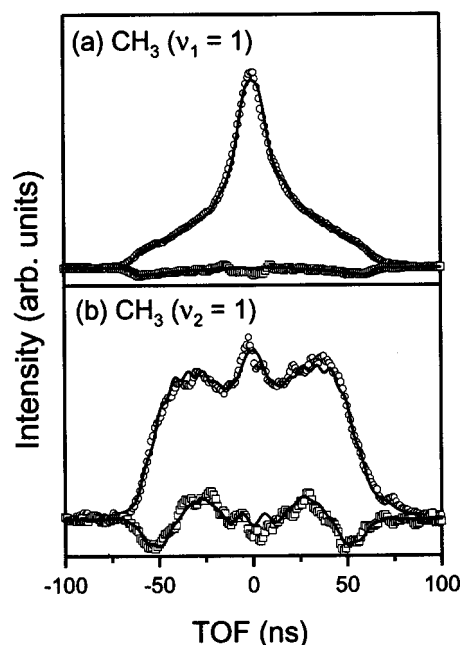


FIG. 4. Isotropic and anisotropic components of the core-extracted TOF profiles of (a) CH₃ ($\nu_1=1$) and (b) CH₃ ($\nu_2=1$). The open circles and squares are the isotropic and anisotropic components of the measured TOF profiles, whereas the solid lines are the results of the fit.

curve at higher velocities. From the measured spatial anisotropy, the speed distribution shown in Fig. 5(a) is decomposed into contributions from the HCl ($\nu=0$) and HCl ($\nu=1$) channels [see Fig. 5(c)]. The low-speed component of the CH₃ ($\nu_1=1$) product is mostly produced with HCl ($\nu=1$), and the high-speed one corresponds to the HCl ($\nu=0$) co-product. Figure 6 shows a similar analysis for the CH₃ ($\nu_2=1$) product. The measured spatial anisotropy closely follows the curve $\beta[v; \text{HCl}(\nu=1) + \text{CH}_3(\nu_2=1)]$ throughout the entire velocity range. We conclude that the CH₃ ($\nu_2=1$) product is produced almost exclusively with the HCl ($\nu=1$) product.

Figure 7 shows the isotropic and anisotropic components of the core-extracted TOF profiles of HCl ($\nu=1, J=1$) [Fig. 7(a)] and HCl ($\nu=0, J=5$) [Fig. 7(b)] obtained using the $R(1)$ line of $F-X(1,1)$ band and the $R(5)$ line of the $F-X(0,0)$ band, respectively. The signal-to-noise ratio prevented us from obtaining TOF profiles of HCl ($\nu=2$) products. TOF profiles of HCl ($\nu=1$) in higher rotational states ($J=4,5$) show only slight variations in shape (not shown). The acquisition of the TOF profiles of HCl ($\nu=0$) product is primarily limited by interference from the rotationally cold HCl ($\nu=0$) impurity background. Only the HCl ($\nu=0$) products with $J>4$ have a large enough signal-to-background ratio to permit us to obtain the TOF profiles of HCl ($\nu=0$) products. The speed distribution and the spatial anisotropy of the HCl ($\nu=1, J=1$) products are shown in Figs. 8(a) and 8(b), respectively. Figure 8(b) compares the spatial anisotropy of HCl ($\nu=1, J=1$) with the expected curves for different modes of methyl co-product vibrational excitation. From the methyl radical REMPI spectrum (shown in Fig. 3), we rule out the presence of ground-state CH₃ co-products; hence, it is not included in the plot. The mea-

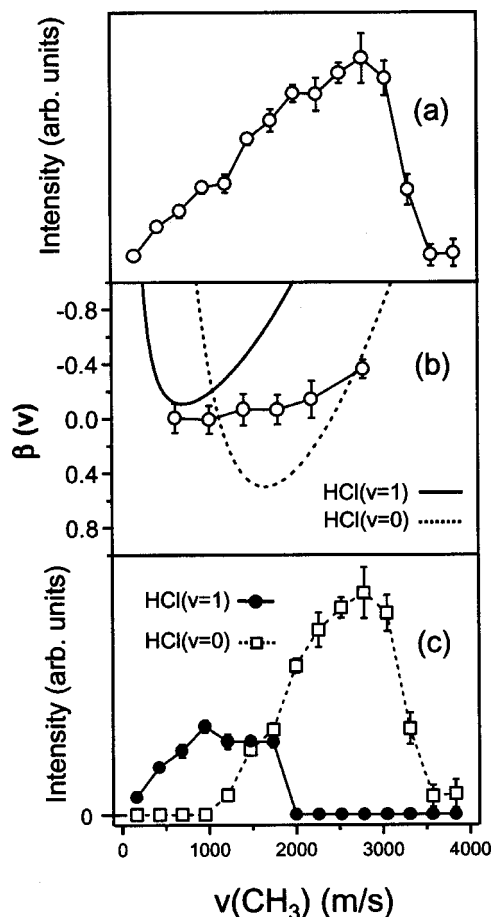


FIG. 5. (a) Speed distribution of CH_3 ($\nu_1=1$) (open circles). (b) Spatial anisotropy of the CH_3 ($\nu_1=1$) product compared with the expected curves for $\text{HCl}(\nu=0)+\text{CH}_3(\nu_1=1)$ (dotted line) and $\text{HCl}(\nu=1)+\text{CH}_3(\nu_1=1)$ (solid line) subchannels. (c) Deconvolution of the speed distribution into two subchannel contributions; $\text{HCl}(\nu=1)+\text{CH}_3(\nu_1=1)$ (solid circles with solid line) and $\text{HCl}(\nu=0)+\text{CH}_3(\nu_1=1)$ (open squares with dotted line).

sured spatial anisotropy follows the curve that is expected for $\text{CH}_3(\nu_2=1)$. However, there is a slight, yet reproducible, deviation from the curve corresponding to the $\text{HCl}(\nu=1)+\text{CH}_3(\nu_2=1)$ channel around the speed range 1–1.5 km/s. Complementary measurements (shown in Fig. 5) on the methyl radical product indicate the existence of $\text{HCl}(\nu=1)$

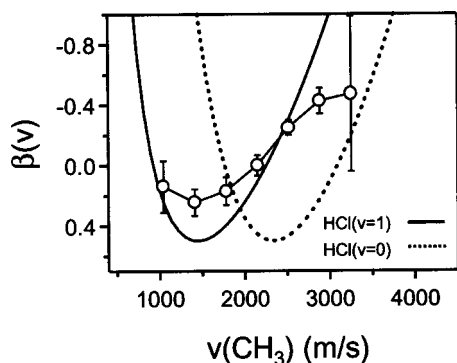


FIG. 6. The spatial anisotropy (open circles) of CH_3 ($\nu_2=1$) compared with the expected curves for $\text{HCl}(\nu=1)$ (solid line) and $\text{HCl}(\nu=0)$ (dotted line) co-products.

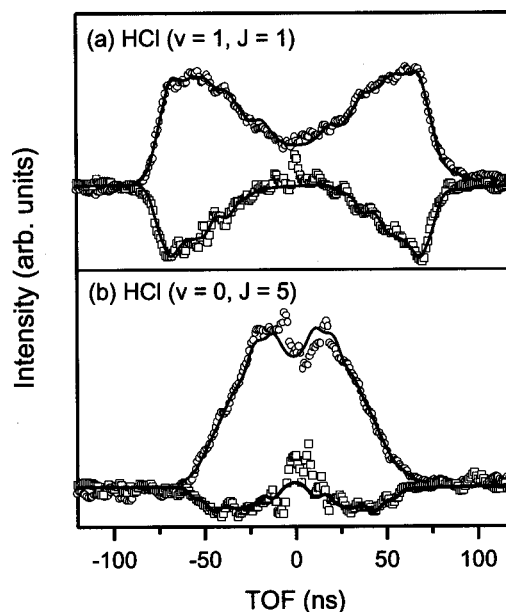


FIG. 7. Isotropic (open circles) and anisotropic (open squares) components of the core-extracted TOF profiles of (a) $\text{HCl}(\nu=1, J=1)$ and (b) $\text{HCl}(\nu=1, J=5)$ products, together with the result of the fit (solid lines).

+ $\text{CH}_3(\nu_1=1)$. Hence, we attribute this deviation to a small contribution from $\text{HCl}(\nu=1)+\text{CH}_3(\nu_1=1)$.²² We estimate an upper bound for this contribution to be 10% of the total $\text{HCl}(\nu=1)$ product. Figure 9 shows the speed distribution and the spatial anisotropy of the $\text{HCl}(\nu=0, J=5)$ product. The measured spatial anisotropy of the $\text{HCl}(\nu=0, J=5)$

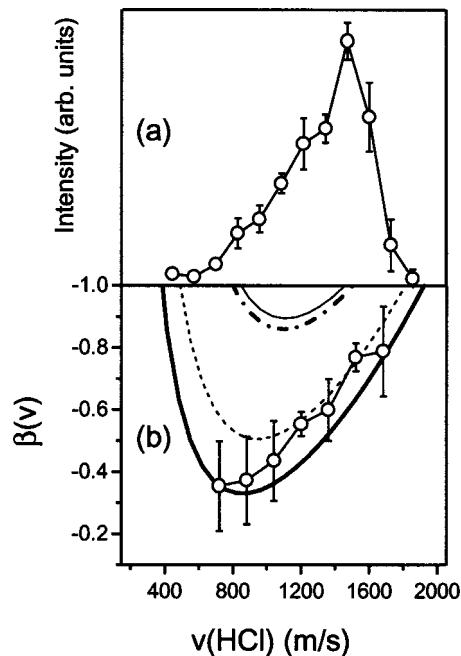


FIG. 8. (a) Speed distribution and (b) spatial anisotropy of the $\text{HCl}(\nu=1, J=1)$ products (open circles). The measured spatial anisotropy is compared with expected curves corresponding to the different modes of vibrational excitation of methyl co-products: umbrella bending (thick solid line), in-plane deformation (thin dotted line), symmetric stretching (thick dashed-dotted line), and asymmetric stretching (thin solid line). The error bars represent $2\sigma_{n-1}$ of replicate measurements.

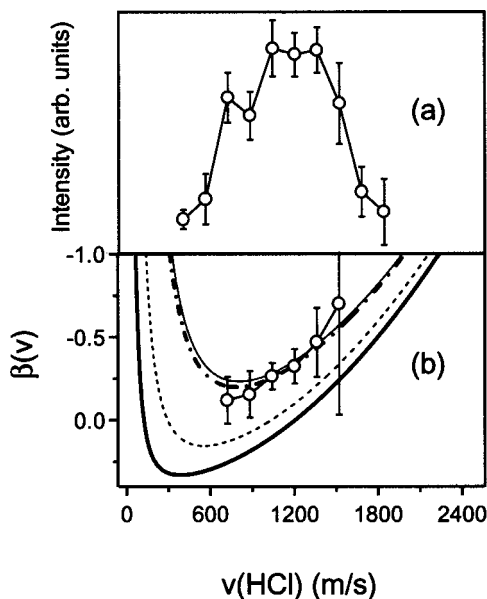
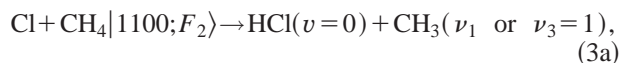


FIG. 9. Results of the analysis on the HCl ($v=0$, $J=5$) TOF profile. (a) The speed distribution. (b) The spatial anisotropy is compared with various modes of CH₃ excitations. Same notations are used as in Fig. 8.

product closely follows the curves that correspond to $\nu_1=1$ or $\nu_3=1$ excited methyl radical within the entire speed range, which is in agreement with the result of the measurement of the CH₃ ($\nu_1=1$) product. We conclude that most of the HCl ($v=0$) products are produced in coincidence with the CH₃ (ν_1 or $\nu_3=1$) products.

In summary, from the measurements of the spatial anisotropies of both HCl and CH₃ products, we identify the following three product channels (in order of importance):



which hereafter are called channels (a), (b), and (c).

C. State-resolved differential cross sections

Figure 10 presents the DCSs for the HCl ($v=0$) and HCl ($v=1$) products obtained from analyses of the speed distributions of HCl and CH₃ products. The DCS for channel (c) is obtained from the deconvoluted speed distribution of the HCl($v=1$) + CH₃($\nu_1=1$) channel shown in Figs. 5(a)–5(c). The differential cross sections show dramatic channel specificity: channel (a) shows side/back scattering; channel (b) shows side scattering; channel (c), which is almost a thermoneutral channel, shows forward scattering. The DCSs for channels (b) and (c) decrease sharply in intensity near the scattering angle, $\cos \theta \sim 0.6$. In later sections, we will show that this cutoff in the angular distribution is consistent with the picture of impulsive energy release along the line of centers.

It is worthwhile to compare our DCSs with those of HCl products from the reaction $\text{Cl} + \text{CH}_4$ ($\nu_3=1$ or $|1000;F_2\rangle$ in local mode notation).¹⁵ The reaction channels Cl

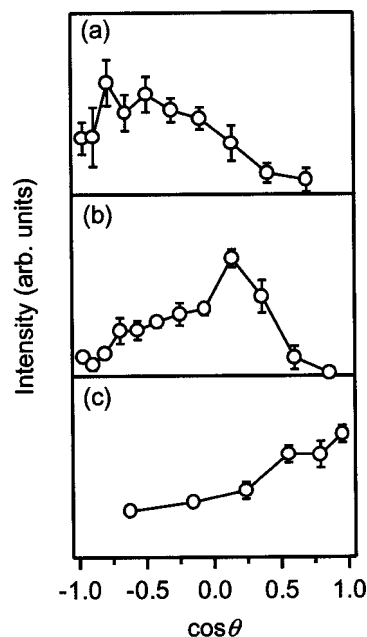


FIG. 10. Differential cross sections of the three identified channels. (a) HCl ($v=0$) + CH₃ (ν_1 or $\nu_3=1$), (b) HCl ($v=1$, $J=1$) + CH₃ ($\nu_2=1$), and (c) HCl ($v=1$) + CH₃ ($\nu_1=1$). To obtain the DCS for channel (b), the contribution from channel (c) was removed from the speed distribution of HCl ($v=1$, $J=1$). The error bars represent $2\sigma_{n-1}$ of replicate measurements.

+ CH₄ $|1000;F_2\rangle \rightarrow \text{HCl}(v=1) + \text{CH}_3(v=0)$ and $\text{Cl} + \text{CH}_4[1100;F_2] \rightarrow \text{HCl}(v=1) + \text{CH}_3(\nu_1=1)$ [channel (c)] have almost the same impulse energy release. Both channels are forward scattered. A similar parallelism also exists between the DCSs of $\text{Cl} + \text{CH}_4[1000;F_2] \rightarrow \text{HCl}(v=0) + \text{CH}_3(v=0 \text{ or } \nu_2=1)$ and of $\text{Cl} + \text{CH}_4[1100;F_2] \rightarrow \text{HCl}(v=0) + \text{CH}_3(\nu_1 \text{ or } \nu_3=1)$ [channel (a)]. This behavior is an indication that only one of the two activated C–H bonds actually participates in the reaction.

D. Rotational polarization of the HCl ($v=1$, $J=1$) product

The scattering-angle resolved alignment moment $A_0^{(2)}$ (STF) for the HCl ($v=1$, $J=1$) product is obtained from the $R(1)$ line of the HCl $F-X$ (1, 1) band. Figures 10(a) and 10(b) show the isotropic $I_{\text{iso}}^{\text{probe}}$ and anisotropic $I_{\text{aniso}}^{\text{probe}}$ components of the TOF profile of HCl ($v=1$, $J=1$). The poor signal-to-noise ratio of the anisotropic component is partly caused by the severe hyperfine depolarization of HCl ($v=1$, $J=1$) that washes out 75% of the initially prepared alignment. From the procedures described in Secs. II C and III, the $A_0^{(2)}$ (STF) moment was obtained as a function of the CM scattering angle, and the results are presented in Fig. 11(c). Overall, the $A_0^{(2)}$ (STF) moments are positive for most scattering angles, and they converge to zero in the backward scattering region. A positive value of $A_0^{(2)}$ (STF) corresponds to a preference for the \mathbf{J}_{HCl} vector to point parallel or anti-parallel to the laboratory velocity vector.

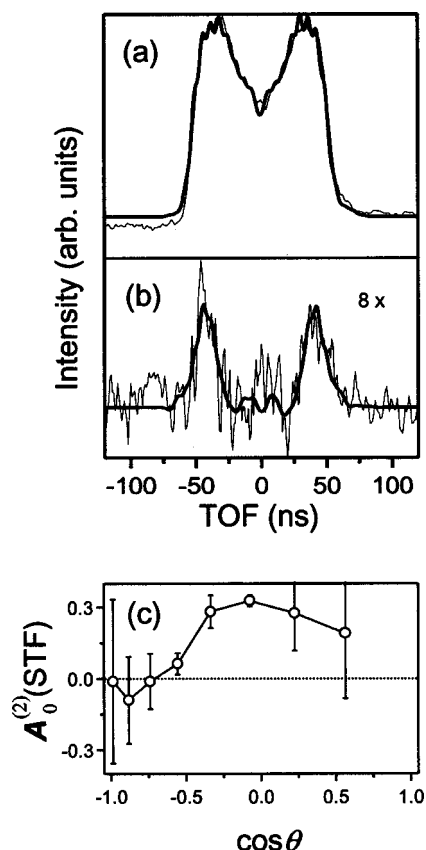


FIG. 11. (a) Isotropic $I_{\text{iso}}^{\text{probe}} = I_{\text{iso}}^{\text{probe}} + 2I_{\text{aniso}}^{\text{probe}}$ and (b) anisotropic $I_{\text{aniso}}^{\text{probe}} = 2(I_{\text{iso}}^{\text{probe}} - I_{\text{aniso}}^{\text{probe}})$ components (thin solid lines) of the TOF profile of HCl ($v=1$, $J=1$), together with the result of fit (thick solid lines). Photolysis polarization is fixed at the perpendicular geometry. (c) Result of analysis, angle-resolved $A_0^{(2)}$ (STF) moment shown as a function of the scattering angle, after correcting for the hyperfine depolarization. The error bars represent σ_{n-1} of replicate measurements.

V. DISCUSSION

A. Rotational excitation of the products

In Sec. IV A, we showed that only a small percentage of energy is channeled into product rotation and most of the energy is deposited in either vibration or translation. The HCl ($v=0$) products are exclusively formed via reaction channel (a) and HCl ($v=1$) products are formed mostly via channel (b) with a small contribution from channel (c), as was shown in Sec. IV B. Therefore the rotational distribution for HCl ($v=0$) represents the dynamics of channel (a). In the same way, the rotational distribution for HCl ($v=1$) represents almost exclusively the behavior of channel (b).

The rotational distribution for HCl ($v=0$) [channel (a)] products shows a remarkable similarity to that of the HCl ($v=0$) products from the $\text{Cl} + \text{CH}_4[1000; F_2] \rightarrow \text{HCl} (v=0) + \text{CH}_3 (v=0 \text{ or } \nu_2)$ reaction. The rotational distribution for HCl ($v=1$) products [mostly via channel (b)] shows a somewhat colder distribution than that of HCl ($v=0$) products. The HCl ($v=2$) rotational distribution is even colder than those of HCl ($v=0$) and HCl ($v=1$) products, and it is primarily restricted by the available energy for the HCl ($v=2$) channel.

Owing to insufficient spectroscopic information on the

1_1^1 and 2_1^1 bands, caused by unresolved rotational lines, we were unable to obtain the rotational distribution of the CH_3 product. We argue, however, that the rotational distribution of the methyl radical is also cold. Assuming that an impulse is released along the reactive C–H bond, a slightly bent transition state of Cl–H–CH_3 will cause both HCl and CH_3 to rotate. However, because the center of mass of CH_3 is located at the central carbon atom, CH_3 should have less torque imparted on it than HCl. Consequently, the degree of rotational excitation should be less for CH_3 than for HCl.

It is tempting to associate the observed cold rotational distributions with the collinear transition state geometry for the hydrogen abstraction reaction. However, the model recently proposed by Picconatto *et al.*²³ warns that this conclusion may not be valid. They propose that the observed cold rotational distributions of the HCl product in $\text{Cl} + \text{CH}_4$ and in related $\text{Cl} + \text{R–H}$ ($\text{R} = \text{C}_2\text{H}_5$, C_3H_6 , etc.) systems are a consequence of the heavy–light–heavy kinematics rather than the linearity of the transition state geometry. Our rotational distributions are within the proposed kinematic limit, providing credibility to the model. However, the rotational distributions are distinctly different for the nearly isoenergetic channels (a) and (b). This behavior indicates that the rotational distribution is not completely determined by the kinematics. We propose an explanation in terms of a difference in the cone of acceptance. If we assume that the dominant reactivity associated with channel (a) is caused by the looser transition state than that of channel (b), it is likely that channel (a) has a wider cone of acceptance, which allows a larger torque to be exerted on the HCl ($v=0$) product. In comparison, channel (b) is less favored (tighter transition state), and therefore has a narrower cone of acceptance, which leads to a colder rotational distribution. In addition, an increased cone of acceptance for channel (a) influences the differential cross section, as we discuss in Sec. V C. Overall, we believe that the rotational distributions of HCl products are determined by the interplay of the heavy–light–heavy kinematics and the geometrically restricted reaction dynamics through its cone of acceptance.

B. Product channels

From the results shown in the preceding sections, it is clear that a general feature of this vibrationally enhanced reaction is that only one of the two activated C–H bonds is strongly coupled to the reaction coordinate, whereas the other activated C–H bond is more or less a spectator. This picture is borne out by the following observations. First, from the REMPI spectrum of CH_3 we found no detectable ground-state methyl radical. Instead, we observed the symmetric stretching band. Second, the vibrational state distribution of HCl indicates a negligible amount of HCl ($v=2$) product. Such products can only occur by extracting two C–H stretching quanta from two spatially separated C–H ($v=1$) oscillators, which is an unfavorable pathway for a direct reaction. Third, all of the HCl ($v=0$) products are produced in coincidence with CH_3 (ν_1 or $\nu_3=1$) [channel (a)], and some of the HCl ($v=1$) products are produced with CH_3 ($\nu_1=1$) [channel (c)]. In both channels, the vibrational

state of the methyl radical product arises from the direct projection of the motion of the vibrationally excited methane. Finally, a striking parallelism exists in the DCSs between the $\text{Cl} + \text{CH}_4[1000; F_2] \rightarrow \text{HCl}(\nu=0,1) + \text{CH}_3(\nu=0 \text{ or } \nu_2=1)$ and $\text{Cl} + \text{CH}_4[1100; F_2] \rightarrow \text{HCl}(\nu=0,1) + \text{CH}_3(\nu_1 \text{ or } \nu_3=1)$ reactions.^{15,22} From these experimental observations, we conclude that a majority [$\sim 73\%$; channels (a) and (c)] of the reaction proceeds without energy redistribution of the excited C–H bonds.

The product channel (b) $\text{HCl}(\nu=1) + \text{CH}_3(\nu_2=1)$ that accounts for approximately 27% of the reaction cannot be explained by a simple, adiabatic picture. In this channel, two C–H stretch quanta (6000 cm^{-1}) of CH_4 are directed into HCl vibration (2991 cm^{-1}) and translation (2400 cm^{-1}), leaving the CH_3 product in the umbrella bending mode (606 cm^{-1}) state. Analogous experiments on $\text{Cl} + \text{CH}_2\text{D}_2$ (Refs. 5 and 24) also show the same behavior, indicating that energy flow is restricted between the two initially excited C–H bonds. One peculiar aspect of this channel is the dominant excitation of the umbrella bending mode in $\text{CH}_3(\nu_2=1)$, instead of the ground state CH_3 . One explanation can be given in terms of the possible role of low-frequency bending mode character either originally present in the eigenstate of CH_4 we prepare,¹⁰ or excited via interaction with the Cl atom. According to Corchado *et al.*,²⁵ the ν_4 mode of CH_4 is closely coupled to the reaction coordinate and adiabatically correlated to the ν_2 (bending) mode of the CH_3 product. Classically, this correlation is equivalent to the geometric change from the pyramidal structure of CH_3 moiety in the transition state to the planar methyl radical product. If we assume that the low-frequency bending mode of CH_4 facilitates the interbond coupling, the products from this nonadiabatic channel will show an enhanced production of the low-frequency bending modes, i.e., the dominant excitation of the umbrella bending mode of the CH_3 product.

Partial breakdown of the spectator bond limit has been observed in systems such as $\text{Cl} + \text{HCN}$ and $\text{Cl} + \text{H}_2\text{O}$,^{26,27} where the breakdown is ascribed to either the formation of a long-lived complex or a fast entrance channel interaction. A recent theoretical model by Fair *et al.*²⁸ suggests that this entrance channel interaction could be particularly significant for molecules with degenerate vibrations such as H_2O or CH_4 . We find that the reaction $\text{Cl} + \text{CH}_4[1100; F_2]$ proceeds largely via vibrationally adiabatic pathways, but some nonadiabatic coupling is likely occurring in channel (b).

C. Channel-specific differential cross sections

As shown in Fig. 9, the angular distributions differ significantly for each HCl product channel. The $\text{HCl}(\nu=0) + \text{CH}_3(\nu_1 \text{ or } \nu_3=1)$ channel (a) is side and backward scattered, the $\text{HCl}(\nu=1) + \text{CH}_3(\nu_2=1)$ channel (b) is side scattered, and the $\text{HCl}(\nu=1) + \text{CH}_3(\nu_1=1)$ channel (c) is forward scattered. In this section, we account for the channel-specific DCSs in terms of a simple hard sphere model. It has been shown that the H-atom abstraction reaction that involves transfer of the H atom away from the center of mass of the polyatomic reagent prefers collisions with high impact parameters. This so-called peripheral

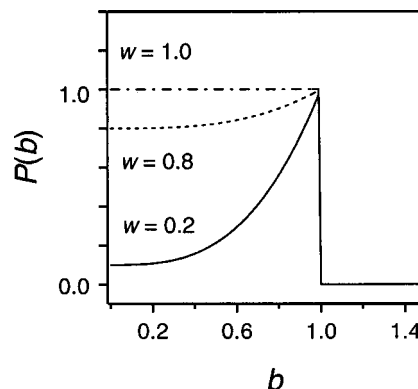


FIG. 12. Model opacity functions [see Eq. (3)] for the description of peripheral dynamics: (a) Peripheral opacity function ($w=0.2$ and $n=3$, solid line), (b) nearly uniform opacity function ($w=0.8$ and $n=3$, dotted line), and (c) hard-sphere opacity function (dashed-dotted line).

dynamics^{29–31} is a consequence of (1) the direct, localized reactivity of the polyatomic reagent, (2) a narrow cone of acceptance around the reactive bond, and (3) the fact that the H atom is far from the center of mass of the polyatomic reagent. On the other hand, a wide cone of acceptance for the reaction will result in an approximately uniform, nonperipheral opacity function. We model the opacity function as follows:

$$P(b; w, n) = (1 - w)b^n + w \quad \text{if } b \leq 1, \\ = 0 \quad \text{if } b > 1, \quad (4)$$

where b is the reduced impact parameter (we set the maximum impact, b_{max} , as 1). The parameter w describes the difference in reactivity between collisions of maximum and minimum impact parameter. If $w=1$, the reaction does not have any preference toward high-impact parameter and corresponds to a simple hard sphere collision (nonperipheral opacity function). On the other hand, $w=0$ represents the maximum differential reactivity between the lowest and the highest impact parameters (peripheral opacity function). The parameter n determines how fast the reactivity converges to the baseline as we move toward lower impact parameters (see Fig. 12). In modeling and interpreting DCSs, we use the parameter w as a measure of the width of the cone of acceptance. Also, we assume that the C–H bond is broken and an impulse is released when Cl and H–CH₃ are in hard-sphere contact. The quasiclassical trajectory calculation by Levine and co-workers³¹ on the $\text{Cl} + \text{CH}_4(\nu_3=1)$ reaction shows the one-to-one correspondence between the impact parameter and the scattering angle expected for hard-sphere collisions. In this reaction, the mass of the H atom is much smaller than the masses of Cl and CH₃. Therefore, for simplicity's sake, we assume that there is an exchange of momentum between the collision partners, but not a change in mass, i.e., the reduced mass of the reagents and the products are the same. The collision of two structureless, hard spheres, $A + B$, with collision radius d and the impact parameter b causes the exchange of momenta along the line of centers (\hat{d} , unit vector) of the two collision partners [see Fig. 13(a)]:

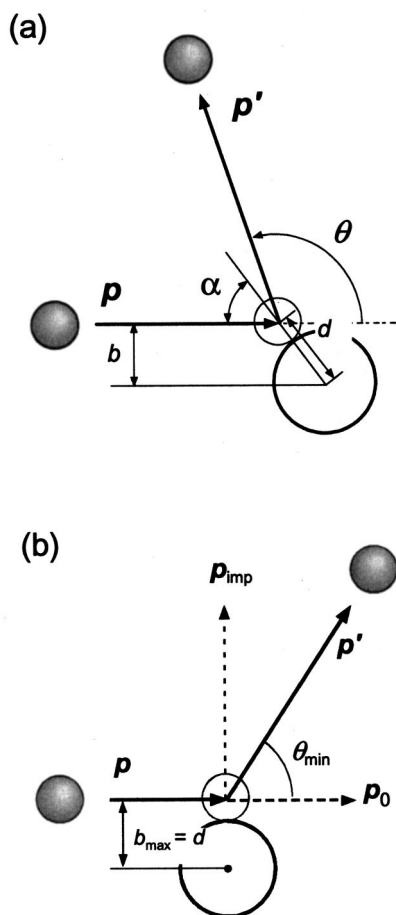


FIG. 13. Hard sphere impulse release model. (a) Collision with impact parameter b , the collision diameter d defines the contact angle, α . The impulse is released along the line of centers, to give the final scattering angle, θ . (b) Near-miss collisions lead to the minimum deflection angle, $\cos \theta_{\min} = 1/(1 + \Delta E/E_0)^{1/2}$, which is determined by the ratio between the impulsive energy release and the initial collision energy.

$$\vec{p}' = \vec{p} - [\vec{p} \cdot \hat{d} + \sqrt{(\vec{p} \cdot \hat{d})^2 + 2\mu\Delta E}] \hat{d}, \quad (5)$$

where $\vec{p} = \vec{p}_A = -\vec{p}_B$ and $\vec{p}' = \vec{p}'_A = -\vec{p}'_B$ are the CM momenta before and after the collision, respectively. In Eq. (5) ΔE is the kinetic energy release upon contact, and μ is the reduced mass of the collision partners. Equation (5) leads to an expression for the scattering angle as a function of impact parameter that is identical to that of the DIPR (direct interaction with product repulsion) model proposed in the context of charge-transfer reactions.^{32–34}

$$\cos \theta = \hat{p}' \cdot \hat{p} = \frac{1}{\kappa} [\sin^2 \alpha - \cos \alpha \sqrt{\kappa^2 - \sin^2 \alpha}], \quad (6)$$

where $\kappa = (1 + \Delta E/E_0)^{1/2}$, $E_0 = p^2/2\mu$, and $\sin \alpha = b/d$. A few points regarding Eq. (6) are in order. For a thermoneutral channel ($\Delta E = 0$), Eq. (6) reduces to the well-known formula for hard-sphere elastic scattering, $\cos \theta = 2(b/d)^2 - 1$. The minimum scattering angle $\cos \theta_{\min}$ for a given impulse, ΔE is achieved with maximum impact parameter [see Fig. 13(b), $\alpha = \pi/2$, $b = b_{\max}$]:

$$\cos \theta_{\min} = 1/\sqrt{1 + \Delta E/E_0}. \quad (7)$$

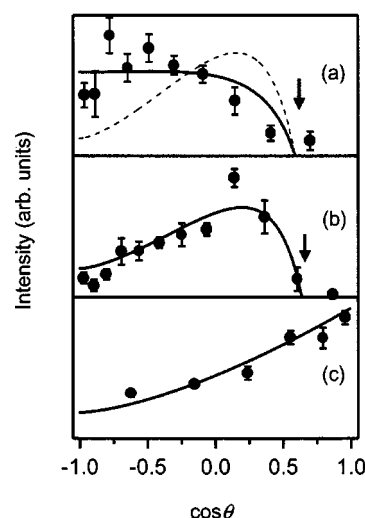


FIG. 14. Comparison of the measured DCSs (solid circles) and the model DCS (solid lines) for three major channels, (a) HCl ($v=0$) + CH₃ (v_1 or $v_3=1$), (b) HCl ($v=1, J=1$) + CH₃ ($v_2=1$), and (c) HCl ($v=1$) + CH₃ ($v_1=1$). For (a), the dashed line corresponds to the case with a peripheral ($w=2$) opacity function. The arrows in (a) and (b) indicate the minimum deflection angles expected from $\cos \theta_{\min} = 1/(1 + \Delta E/E_0)^{1/2}$.

Note that $\cos \theta_{\min}$ is dependent only on the relative amount of the impulsive energy release, and Eq. (7) suggests that a minimum deflection trajectory is a result of a simple (orthogonal) vector sum of the velocity vectors associated with impulse release (\vec{p}_{imp}) and the elastic components (\vec{p}_0). With a negligible impulse release, it is possible to have forward-scattered products. However, with significant impulse release, a minimum amount of deflection is required. In general, the impulse need not be released at the time of hard-sphere contact, in which case the limiting behavior of the scattering angle does not necessarily hold. The differential cross section can be readily obtained by the following relationship:

$$\frac{d\sigma}{d \cos \theta} = 2\pi b P(b) \left(\frac{d \cos \theta}{db} \right)^{-1}. \quad (8)$$

Figure 14 compares differential cross sections from our model with the experimental data. In modeling the DCSs, we used the parameters for the opacity functions, $w=0.8$ (flat-top) for channel (a) and $w=0.2$ (peripheral type) for channels (b) and (c), with $n=3$ for all three channels (see Fig. 12). Overall, our model successfully captures the general features of each channel for the (a) HCl ($v=0$) + CH₃ (v_1 or $v_3=1$) and (b) HCl ($v=1$) + CH₃ ($v_2=1$) channels, a significant impulse is released into product translation ($\Delta E/E_0 \sim 2$), which deflects the trajectory of the product away from the initial direction, leading to side and back scattering; for the thermoneutral channel, (c) HCl ($v=1$) + CH₃ ($v_1=1$), little impulsive energy release occurs. Therefore, the propensity for collisions with high-impact parameters leads to forward scattering. Both the DCSs of channels (a) and (b) show a sharp drop in intensity near $\cos \theta=0.6$. This behavior is in remarkable agreement with the predicted minimum scattering angle, $\cos \theta_{\min}=0.59$ for channel (a) and $\cos \theta_{\min}=0.64$

for channel (b), which is consistent with our hypothesis that the H-atom abstraction occurs along the line of centers. The rupture of the C–H bond before or after the hard sphere contact leads to larger or smaller limiting scattering angles, respectively.

The angular distribution for channel (a) is better modeled by a “flattop” ($w=0.8$) opacity function than by opacity function of the peripheral ($w=0.2$) type (see Figs. 12 and 14). On the other hand, channels (b) and (c) can be modeled by the same peripheral opacity function ($w=0.2$). We conclude that the cone of acceptance for channel (a) is significantly wider than those for channels (b) and (c). In other words, this reaction channel has a more relaxed (looser) transition-state geometry. An increased cone of acceptance necessarily causes the opacity function to be less peripheral, which leads to an increased probability for the reaction with low impact parameters. This hypothesis of relaxed transition-state geometry for channel (a) is also consistent with the slightly hotter rotational distribution for channel (a) than for channel (b), as discussed in Sec. V A. It is worth while to note that the DCS for the vibrationally nonadiabatic channel (b) is consistent with our hard-sphere impulse release model and has a narrow cone of acceptance for the reaction. This consistency, together with the cold rotational distribution, indicates that the transition state for this channel is restricted to be collinear and the vibrational energy is redistributed instantaneously.

In summary, the overall agreement of our model with the data confirms the picture that the rupture of C–H bond occurs along the line of centers at the point of hard sphere contact. The observed channel specificity of DCS results from the combined effect of the differences of cone of acceptance and the degree of impulse release that deflects the trajectory away from the forward scattered region.

D. Rotational polarization of the HCl ($v=1$, $J=1$) product

If we assume that the rotational excitation of the product is caused by the torque imparted to the HCl moiety at the transition state, the distribution of the rotational angular momentum vector should be perpendicular to the impulse release direction. Furthermore, the distribution should be cylindrically symmetric with respect to the impulse release direction. For the HCl ($v=1$, $J=1$) product, this behavior is represented by three alignment moments $A_0^{(2)}(\mathbf{F}) < 0$, $A_1^{(2)}(\mathbf{F}) = 0$, and $A_2^{(2)}(\mathbf{F}) = 0$, where \mathbf{F} stands for the reference frame, with the z axis parallel to the axis of cylindrical symmetry. We consider the following three limiting cases for the cylindrical symmetry axis: it lies along \mathbf{u}_{CM} , or along \mathbf{u}_{HCl} , or along the line of centers (\hat{d}). The symmetric J -vector distribution around the vector \mathbf{u}_{CM} or \mathbf{u}_{HCl} corresponds to the cases when the HCl products are formed near the entrance channel or the exit channel, respectively, whereas the symmetric J distribution around the line of centers corresponds to the formation of HCl along the line of centers. Figure 15 shows the comparison of these three cases in the STF frame with the observed $A_0^{(2)}$ (STF) moment of HCl ($v=1$, $J=1$). Our data shows good agreement with the curve corresponding to $A_0^{(2)}(\hat{d}) = -0.6$. The agreement be-

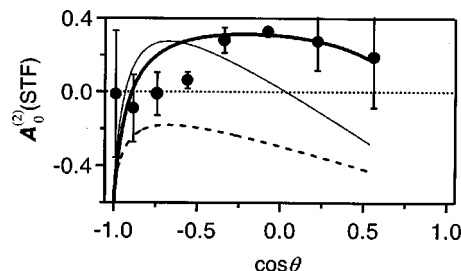


FIG. 15. Comparison of the measured $A_0^{(2)}$ (STF) alignment of HCl ($v=1$, $J=1$) (solid circles) and the expected STF moments of the three limiting cases: $A_0^{(2)}(\mathbf{u}_{\text{HCl}}) = -0.6$ (thin solid line), $A_0^{(2)}(\mathbf{u}_{\text{CM}}) = -0.6$ (dashed line), and $A_0^{(2)}(\hat{d}) = -0.6$ (thick solid line).

tween the model and the data is poor in the backward scattered direction. This discrepancy likely is caused by interference from the off-diagonal moments that we neglected in our analysis. The measured alignment moment of HCl ($v=1$, $J=1$) again agrees with our picture that the H-atom transfer occurs along the direction of the line of centers.

VI. CONCLUSIONS

In this work, we have determined the correlated energy disposal, and the product differential cross sections of the reaction $\text{Cl} + \text{CH}_4[1100; F_2] \rightarrow \text{HCl} + \text{CH}_3$. The internal energy distributions and the correlated energy disposal of HCl and CH₃ products show that the majority of the products are formed without significant energy redistribution of the initially prepared motion of the CH₄. We have also identified the minor, vibrationally nonadiabatic channel HCl ($v=1$) + CH₃ ($v_2=1$). We propose that the low-frequency bending mode character (ν_4) of CH₄ promotes this nonadiabatic

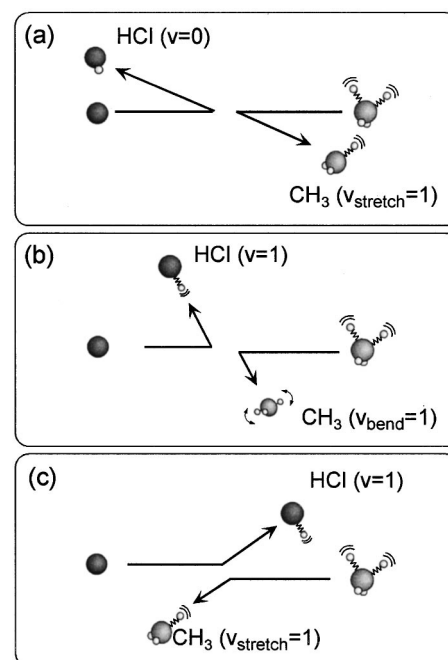


FIG. 16. Schematic for the observed channel-specific scattering behavior of atomic chlorine reacting with the first overtone excited methane: (a) HCl ($v=0$) + CH₃ (ν_1 or $\nu_3=1$), (b) HCl ($v=1$, $J=1$) + CH₃ ($\nu_2=1$), and (c) HCl ($v=1$) + CH₃ ($\nu_1=1$).

TABLE II. Correction factors^a for the *R*-branch lines of 2 + 1 REMPI HCl *F*–*X* (1,2) transitions.

<i>J</i>	<i>C</i> (<i>J</i>)
1	35
2	28
3	32
4	52

^aPopulation of HCl (*v* = 2, *J*) = Signal(*J*) × *C*(*J*) / (UV probe power)².

channel. The angular distributions for three identified channels and the scattering-angle-resolved rotational alignment moment show that the H atom is transferred, and hence impulse is released along the hard-sphere line-of-centers direction (see Fig. 16). Our results clearly demonstrate that the direct and local mode picture of the chemical reaction remains largely valid for the reaction involving vibrationally excited methane.

ACKNOWLEDGMENTS

One of the authors (H.A.B.) thanks the National Science Foundation for a graduate fellowship. We thank Jon P. Camden for useful discussions and critical comments on the paper. This work was supported by the National Science Foundation under the Grant No. NSF-CHE-99-00305.

APPENDIX: CORRECTION FACTORS FOR HCl *F*–*X* (1, 2) TRANSITIONS

The correction factors for the *F*–*X* (1, 2) transitions were experimentally obtained by pumping a single HCl rotational line of the *v* = 2 ← *v* = 0 overtone transition with an IR beam. Table II lists the ratios of the enhanced HCl (*v* = 2, *J*) signal and the depleted HCl (*v* = 0, *J'*) signal that were obtained using the *F*–*X* (1, 2) and *F*–*X* (0, 0) 2 + 1 REMPI schemes. These ratios are corrected for the difference in UV probe power, and multiplied by the published correction factors for the *F*–*X* (0, 0) transition.¹⁵ It must be warned that due to the significant intensity-dependent ion fragmentation, difference in power density or focusing condition of the REMPI laser beam can change the correction factors.

¹R. N. Zare, *Science* **279**, 1875 (1998).

²F. F. Crim, *Acc. Chem. Res.* **32**, 877 (1999).

³M. J. Bronikowski, W. R. Simpson, and R. N. Zare, *J. Phys. Chem.* **97**, 2194 (1993).

⁴A. Sinha, M. C. Hsiao, and F. F. Crim, *J. Chem. Phys.* **94**, 4928 (1991).

⁵Z. H. Kim, H. A. Bechtel, and R. N. Zare, *J. Am. Chem. Soc.* **123**, 12714 (2001).

⁶F. Menard-Bourcin, L. Doyennette, J. Menard, and C. Boursier, *J. Phys. Chem. A* **104**, 5444 (2000).

⁷R. Z. Martínez, D. Bermejo, J. Santos, J. P. Champion, and J. C. Hilico, *J. Chem. Phys.* **107**, 4864 (1997).

⁸T.-K. Ha, M. Lewerenz, R. Marquardt, and M. Quack, *J. Chem. Phys.* **93**, 7097 (1990).

⁹L. Halonen and M. S. Child, *Mol. Phys.* **46**, 239 (1982).

¹⁰L. Halonen, *J. Chem. Phys.* **106**, 831 (1997).

¹¹M. Lewerenz and M. Quack, *J. Chem. Phys.* **88**, 5408 (1988).

¹²R. Atkinson, D. L. Baulch, R. A. Cox, R. F. Hampton, J. A. Kerr, and J. Troe, *J. Phys. Chem. Ref. Data* **21**, 1125 (1992).

¹³A. J. Orr-Ewing, W. R. Simpson, T. P. Rakitzis, S. A. Kandel, and R. N. Zare, *J. Chem. Phys.* **106**, 5961 (1997).

¹⁴T. P. Rakitzis, S. A. Kandel, T. Lev-On, and R. N. Zare, *J. Chem. Phys.* **107**, 9392 (1997).

¹⁵W. R. Simpson, T. P. Rakitzis, S. A. Kandel, A. J. Orr-Ewing, and R. N. Zare, *J. Chem. Phys.* **103**, 7313 (1995).

¹⁶P. C. Samartzis, B. Bakker, T. P. Rakitzis, D. H. Parker, and T. N. Kitso-poulos, *J. Chem. Phys.* **110**, 5201 (1999).

¹⁷A. Yokoyama and T. Takayanagi, *Chem. Phys. Lett.* **307**, 48 (1999).

¹⁸R. N. Zare, *Angular Momentum* (Wiley, New York, 1988).

¹⁹J. W. Hudgens, T. G. DiGiuseppe, and M. C. Lin, *J. Chem. Phys.* **79**, 571 (1983).

²⁰D. W. Chandler, J. W. Thoman, M. H. M. Janssen, and D. H. Parker, *Chem. Phys. Lett.* **156**, 151 (1989).

²¹R. O. Loo, H.-P. Haerri, G. E. Hall, and P. L. Houston, *J. Chem. Phys.* **90**, 4222 (1989).

²²It might be wondered how the *ν*₁ (symmetric stretch) excited CH₃ could result from the direct projection of the eigenstate |1100;*F*₂⟩ of CH₄. It may also appear that only the *ν*₃ (asymmetric stretch) excited CH₃ correlates to |1100;*F*₂⟩ upon increasing the C–H bond distance. However, it must be noted that the eigenstate, |1100;*F*₂⟩ of the CH₄ is triply degenerate and is a (properly symmetrized) linear combination of (unsymmetrized) local mode basis set, {|*n*₁*n*₂*n*₃*n*₄⟩}. Removal of one H atom breaks this degeneracy and leads to excitation of both the *ν*₁(*A*₁) and *ν*₃(*E*) modes of CH₃. In this regard, we expect that CH₃ products are also excited in the *ν*₃ mode as well as the *ν*₁ mode. We were not able to find a band that can be assigned to the *ν*₃ band in the REMPI spectrum of CH₃, and there appears to be no spectroscopic report on the observation of the *ν*₃ band via the 3*p*_z–*X* REMPI transition [J. W. Hudgens (private communication)]. However, this fact does not allow us to rule out the existence of *ν*₃-mode-excited methyl radicals.

²³C. A. Picconatto, A. Srivastava, and J. J. Valentini, *J. Chem. Phys.* **114**, 1663 (2001).

²⁴H. A. Bechtel, Z. H. Kim, J. P. Camden, and R. N. Zare (unpublished).

²⁵J. C. Corchado, D. G. Truhlar, and J. Espinosa-Garcia, *J. Chem. Phys.* **112**, 9375 (2000).

²⁶A. Sinha, M. C. Hsiao, and F. F. Crim, *J. Chem. Phys.* **94**, 4928 (1991).

²⁷A. Sinha, J. D. Thoenke, and F. F. Crim, *J. Chem. Phys.* **96**, 372 (1992).

²⁸J. R. Fair, D. Schaefer, R. Kosloff, and D. J. Nesbitt, *J. Chem. Phys.* **116**, 1406 (2002).

²⁹P. M. Aker and J. J. Valentini, *Isr. J. Chem.* **30**, 157 (1990).

³⁰M. Ben-Nun, M. Brouard, J. P. Simons, and R. D. Levine, *Chem. Phys. Lett.* **210**, 423 (1993).

³¹X. Wang, M. Ben-Nun, and R. D. Levine, *Chem. Phys.* **197**, 1 (1995).

³²M. T. Marron, *J. Chem. Phys.* **58**, 1973 (1973).

³³P. J. Kuntz, *Trans. Faraday Soc.* **66**, 2980 (1970).

³⁴P. J. Kuntz, M. H. Mok, and J. C. Polanyi, *J. Chem. Phys.* **50**, 4623 (1969).

³⁵W. J. van der Zande, R. Zhang, R. N. Zare, K. G. McKendrick, and J. J. Valentini, *J. Phys. Chem.* **95**, 8205 (1991).